The spatiotemporal richness of hummingbird wing deformations

Dimitri A. Skandalis[1,2,*], Vikram B. Baliga[1], Benjamin Goller[1,3], Douglas A. Altshuler[1,†]

[1] Department of Zoology, University of British Columbia

Current affiliations: [2] Psychological and Brain Sciences & Johns Hopkins Kavli Neuroscience Discovery Institute, Johns Hopkins University; [3] College of Agriculture Data Services, Purdue University

[*] corresponding author: da.skandalis@gmail.com

[†] corresponding author: doug@zoology.ubc.ca

Keywords: shape, flight, plasticity, dynamics

ABSTRACT

Animals exhibit rich diversity in form, including in tissues whose function depends on deforming. In fluidic locomotion, deformations contribute to aspects of performance ranging from propulsive efficiency to environmental navigation, but it is challenging to quantify and compare dynamic morphological variation. There are many possible ways to quantify morphology but their correspondence to dynamic variation among distinct behaviours is unclear. We contrasted dynamic wing shape variation of hoverfeeding hummingbirds during distinct flight challenges to assess how morphological plasticity contributes to their aerial agility. We sought to quantify the principal axes of shape variation (shape variables) and their relationships to conventional descriptors of wing shape like wing twist and area. The first four shape variables collectively explained >95% of the dynamical variation in wing shape and decomposed shape changes into a frequency spectrum of in- and out-of-plane deformation components. To varying degrees, these shape variables were interpretable as aspects of conventional two- and three-dimensional morphology, particularly the dominant contributions of wing twisting (~80% of shape variation) and area changes (~10% of shape variation). However, variation in wing morphology among behaviours was not predicted by each shape variable's explained variance, but instead by stroke cycle subintervals associated with specific shape changes. We identified pronounced out-of-plane deformations throughout the stroke cycle while hoverfeeding in front of a visual barrier, whereas in-plane deformations during the upstroke and pronation were especially prominent during submaximum load lifting. Our study highlights the complexity of shape changes in biological tissues during active behaviour, and how dynamic morphology contributes to agile fluidic locomotion.

INTRODUCTION

Behavioural plasticity is central to animals' successes in adapting to a wide range of environments. Through changes in behaviour, animals can operate freely in diverse habitats and exploit a wider range of resources. In soft-bodied organisms, plasticity encompasses deformations of body shape due to passive environmental and active muscular loads. Deformations arise from behavioural, environmental, and evolutionary factors and contribute to motor control, propulsive efficiency, and the metabolic cost of locomotion and scope for power modulation among behaviours (Aiello et al., 2017; Akanyeti et al., 2016; Lehmann et al., 2011; Lucas et al., 2014; Mountcastle and Combes, 2013; Skandalis et al., 2017; Tytell et al., 2016; Zheng et al., 2013). The timing and control of deformations during flapping locomotion is critical for modulating forces but can also impact diverse organismal functions like environmental sensing and respiratory cycles (Akanyeti et al., 2016). Despite the importance of deformations for performance, the incredible diversity of animal shapes and kinematics poses a challenge for quantifying the scope of shape changes across the behavioural repertoire. Anatomical studies alone only weakly hint at this range, as for example the observation that birds' joint ranges of motion are less phylogenetically conserved than the individual elements of the wing skeletal morphology (Baliga et al., 2019). To execute behaviours, animals can ostensibly adopt a continuous spectrum of wing, fin, or tail configurations at any interval of the motor cycle, further increasing the difficulty in quantifying shape changes and their roles. There are many potential morphological descriptors derived from posed specimens or rigid aircraft theory, but the extent to which any element of this set adequately explains the complexity of animal shape variation is unclear. Ultimately, understanding shape variation *in vivo* is essential for deciphering both the mechanisms of behavioural flexibility and the elements of organismal evolution.

Locomotor diversity and behavioural flexibility are manifested through the dynamics of force production, so fluid dynamic theory predicts some aspects of morphology that should receive special attention. Airframes of very different sizes and shapes are typically compared through force coefficients C_F. The force coefficients are obtained by normalizing the produced force F to some reference kinematics and morphological configurations represented in the dynamic pressure q and the wing planform area S,

$$C_F = \frac{F}{q \cdot S} = \frac{F}{\frac{1}{2}\rho\dot{\varphi}^2 R_2^2 \cdot S} \qquad \text{eq 1}$$

where the dynamic pressure can be resolved into the products of air density ρ, angular velocity $\dot{\varphi}$, and the radius of the second moment of wing area, R_2 (Ellington, 1984a; Kruyt et al., 2014; Skandalis et al., 2017). Constant C_F implies dynamic similarity of force generation, such that differences in force

production result from some scaling of the underlying dimensional quantities (Skandalis et al., 2017). However, it is not necessarily straightforward to map even wing dimensions of posed specimens to the complex postures that animals adopt in flight, let alone subtle aspects of wing shape (Riskin et al., 2010). In general, C_F varies over the course of the stroke cycle and between behaviours, so identifying the mechanisms underlying changes in force production requires detailed knowledge of kinematics and morphology. To fully appreciate the diversity of animal force generation, it will therefore be helpful to understand the spatiotemporal deformations of the wing among behaviours and associate these with common descriptors of morphology, such as those in eq 1.

Behavioural flexibility blurs the distinction between kinematics and morphology implied by considerations of rigid-wing aircraft (eq 1), because both the dimensions and shape are constantly changing along with the motions of the whole wing. In studying the deformations associated with naturalistic locomotor behaviours like navigating turbulence or varying travel speed (Badger et al., 2019; Boerma et al., 2019; Cheney et al., 2020; Gillies et al., 2011; Hubel et al., 2012; Konow et al., 2017; Ravi et al., 2015; Ravi et al., 2020; Reynolds et al., 2014; Standen and Lauder, 2005; Swartz et al., 2006; Thomas, 1996; Tobalske et al., 2007), there remains the significant problem of defining what aspects of shape fully capture behavioural flexibility. Often, shape is examined through ratios of dimensions or angles between them. Examples include the aspect ratio (ratio of area and length), the distribution of surface area with respect to the base, the bending angle of the fin or wing tip, or some indices developed to describe specific aspects of shape like tip roundedness (Ellington, 1984a; Kruyt et al., 2014; Lockwood et al., 1998; Lucas et al., 2014). Some non-dimensional morphological parameters are well-studied in engineering contexts and have proven useful for understanding morphological flexibility. Wing twist, the change in angle from tip to base, is an essential factor in determining the propulsive efficiency of rotating and flapping wings (Ingersoll et al., 2018; Leishman, 2000; Zheng et al., 2013). Camber, the maximum height deviation of a propulsor section, allows lifting surfaces to generate greater weight-supporting forces at lower flight speeds; both birds and bats have been observed to rely on cambering in slow flight (Muijres et al., 2008; Muijres et al., 2012). However, as the degrees of freedom in wing control increase, so too does the complexity of the resulting shape. Bats exhibit great individual variation in the combinations of kinematics and wing shapes they can adopt in typical flight, and the shape variation further diverges across flight speeds or during force loading (Iriarte-Diaz et al., 2012). Whether the metrics of shape capture all this variation between behaviours and among individuals is unclear. Given the diversity of *dynamical* wing shapes (varying over time) among and within species, we may expect that metrics of shape and size derived from aerodynamic models (e.g., (Ellington, 1984a)) may apply better to some animal groups than others. Understanding the correspondence between our shape measures and real

behaviour will therefore be essential for inferring broad evolutionary patterns in animal performance (e.g., (Norberg and Rayner, 1987; Rayner, 1988)).

The complexity and difficulty of adequately describing wing shape deformations leads us to consider data-driven approaches for discovering basis functions that capture the principal types of shape variation throughout the stroke cycle. Past work has adopted a similar approach in applying singular value decomposition of body-centric (Bartol et al., 2018; Riskin et al., 2008) or displacement coordinates (Bozkurttas et al., 2009) of natural (e.g., joint positions) and artificial (e.g., painted) markers. This approach provides a reduced rank approximation of the shape variation to ease comparisons of major elements of deformations. However, because the marker trajectories are decomposed directly, the principal axes of variation will be oriented along the lines of greatest kinematic deviation, such as the flapping stroke plane. Consequently, we refer to these axes as kinematic modes. Although shape changes contribute to kinematic modes, it is not possible to differentiate between any notions of kinematics and morphology corresponding to our usual view of fin or wing shapes, such as those obtained by posing. One approach to separating morphology and kinematics is to define shape as the information that remains after accounting for rigid transformations between successive time steps (Kendall, 1984). Thus, we can obtain a set of *shape variables* by performing modal decompositions after removing symmetries due to translation, scaling, and rotation. Through this approach, the recovered shape variables will correspond to in- and out-of-plane deformations. Moreover, we can then examine the concordance between our shape variables and some set of morphological descriptors, such as the twist and camber profiles. Where there is a strong alignment, we can infer that our typical descriptors adequately explain biological variation. Conversely, we can infer from a weak correspondence that there are biologically meaningful deformations that have yet to be well described, and which can therefore inspire new insights into propulsion with flexible materials.

Here, we study wing shape variation in Anna's hummingbird (*Calypte anna*) as a model of morphological plasticity within stroke cycles and across flight behaviours. Hummingbirds are spectacularly agile and can generate burst forces several times their body weight through kinematic modulation, but whether wing shape variation contributes to maneuvering flight is poorly described (Ravi et al., 2020; Read et al., 2016; Segre et al., 2015; Skandalis et al., 2017). In part, this may be because hummingbirds appear to exhibit much less shape variation than birds with distally morphing wings [large span ratios; (Baliga et al., 2019; Riskin et al., 2012; Stowers et al., 2017; Tobalske et al., 2007)]. However, at the high wing beat frequencies of hummingbirds, the timing of shape and dimensional changes may be as important as their magnitude. We therefore examined the dynamics of wing shape changes over the stroke cycle as hummingbirds were challenged to fly in front of a visual mask and

during submaximum load lifting. Hummingbirds adapt their stroke kinematics to these challenges, such as through greatly reduced or increased stroke amplitudes respectively (Mahalingam and Welch, 2013; Wells, 1993), but whether wing shape changes as well is unclear. We tracked a dense set of markers through multiple stroke cycles and inferred spatiotemporal patterns of wing deformations using well-known biological measurement techniques (geometric morphometrics) that have not frequently been applied to dynamic shapes in locomotion (but see (Adams and Cerney, 2007), or e.g., (Qiu et al., 2009) for approaches to computational anatomy in similar contexts). We derived a set of shape variables from the marker tracking data that described most of the shape variation in typical hoverfeeding flights and identified correspondences both to morphological descriptors in the literature and to identifiable subintervals of the stroke cycle, such as the mid-half stroke and stroke reversal configurations. Through these shape variables, we identified distinct spatiotemporal profiles of wing shapes among flight behaviours, and how morphing bodies expand the hummingbird performance envelope.

METHODS

Wing and body marking

Five male *Calypte anna* were wild caught on the campus of the University of British Columbia and housed in an animal care facility. All procedures were approved by the University of British Columbia Animal Care Committee in accordance with the guidelines set out by the Canadian Council on Animal Care. Marker placement dictates what aspects of shape variation can be quantified, such as joint positions (Hedrick et al., 2012; Riskin et al., 2008), the wing perimeter (Ingersoll et al., 2018; Song et al., 2014), fin ray and feather rachis deflection (Bozkurttas et al., 2009; Maeda et al., 2017; Standen and Lauder, 2005), or marker- and markerless reconstructions of internal surfaces (Bachmann et al., 2012; Cheney et al., 2020; Cheney et al., 2022; Deetjen et al., 2017; Gillies et al., 2011; Heinold and Kähler, 2015; Walker et al., 2009; Windes et al., 2018). Most hummingbird wings are featureless and have few landmarks, unlike the veins and patterns on insect wings (Koehler et al., 2012; Le et al., 2013; Phan et al., 2017; Young et al., 2009) and so three-dimensional reconstructions necessitate dense application of markers over the entire wing (Windes et al., 2018). For our desired marker density, painting (e.g., titanium dioxide, (Song et al., 2014)) introduces handling stress, mechanically disrupts preening and wing integrity by interfering with the interlocking barbules (Matloff et al., 2020), and adds inertia, all of which may substantially disrupt aerodynamics and sensory feedback and alter typical flight patterns. Instead, we devised a weightless marker technique (the ‘hummingbird salon’) that yielded long-lasting and weightless markers and afforded substantial time for the animal to recover prior to experiments. We bleached spots on the surface of the wing with a commercially available hair bleach foaming agent, L'Oréal Paris®

Perfect Blondissima Crème™ (because they're worth it). Awake birds were gently restrained in a tensor bandage with a slot for one wing and laid in a foam cradle with the wing extended through gentle pressure on the outer primaries. We applied at least three dots of bleaching foam to each feather, generally along the rachis of the feather, and on selected dorsal covert feathers. The sixth secondary flight feather (S6) was absent or infrequently visible among birds, and so excluded. The bleaching agent was allowed to dry for at least five minutes, and then thoroughly soaked and rinsed with multiple washes of tap water to ensure that bleaching agent residue could not be ingested by a preening bird. We did not observe any difference in health or flight capacity between marked and unmarked birds in our population. The entire marker set was applied over multiple sessions of about 30 minutes to limit handling stress to the bird. Both marking experience and the small size of the animal relative to the restraining hands led to some differences in the number and placement of markers, resulting in 58-64 markers over the whole wing. This marking technique is not practical on the body feathers because of low contrast and large feather displacement compared to flight feathers. Instead, we applied five white paint spots (Bic® Wite-Out or Paper Mate® Liquid Paper) to the bird's back on the day of experimentation. The mass of these spots is minor compared to the body inertia (about 0.07 mg).

Marker tracking

Markers were manually tracked from at least four colour high-speed camera views (one Miro4 and three Miro120s, Vision Research, Inc.), filming at 2200 Hz and 512x512 pixel resolution. Depending on availability, we also used a greyscale Phantom v12.1 and Phantom v311 (Vision Research, Inc.). Camera frame synchronisation was controlled by a function generator (Tektronix AFG3021B), and shutter time was a maximum of 150 μs, depending on the camera's capabilities and lens aperture. We used 24-, 32-, and 50-mm lenses, and due to the sensor crop factor and small image size in the center of the lens, nonlinear image distortions were negligible. Cameras were calibrated using direct linear transform coefficients (Hedrick, 2008) determined by a physical calibration object or through sparse bundle adjustment (Theriault et al., 2014). The gravity vector was determined from the suspended physical calibration object's +Z axis or by dropping a bead through the cameras' fields of view. Feather motions and variation in lighting through the stroke cycle sometimes resulted in ambiguous marker positions. Where possible, the marker position was estimated based on nearby markers, or for short gaps of a few frames, the position was interpolated by a smoothing spline. Otherwise, the marker for that individual was deleted from the dataset. Markers at the wing base (secondary flight feathers) were most affected but are densely packed, limiting the impact on reconstruction. The digitisation precision of each marker in each frame was estimated by the reprojection error of the reconstructed 3D position. We enforced a minimum digitising root mean square error (RMSE) of 1, and the marker standard deviation

was calculated by bootstrapping (100 iterations) the residual error in each camera view and recalculating the 3D reconstructed position. The smoothed marker positions were then found by a cubic spline weighted by the relative standard deviations of all points in the time series. This fitting procedure resulted in the smoothest function consistent with the marker positions and the digitising error. The smoothing method is implemented in a custom Matlab package (Hedrick, 2008).

Overall, the appearance of spatiotemporal features of marker motions depends on the quality of evidence (e.g., number of camera views on marker, precision of calibration, digitisation precision). High frequency features, such as rapid displacements, require more evidence and denser spatial and temporal sampling. Enforcing a minimum digitising error therefore amounts to a low-pass filter dependent on the magnification of the marker in each camera view since the pixel error will translate to a larger uncertainty for less magnified markers. Consequently, sharp positional changes without strong evidence will be smoothed out. In terms of shape reconstruction, our labelling and tracking method is consequently conservative (type I error) and may miss some real features (type II error).

Hovering flight challenges

The experimental flight chamber was made of five panels of clear acrylic measuring 52 cm on each side, with the bottom panel covered by a thin 1 cm^2 mesh to prevent recirculation of the downwash. The tip of a custom feeder was centrally placed 18 cm and >3 wing lengths from the wall (based on average *C. anna* wing length 5.5 cm). The feeder mouth was extended with a tube ~1.5 cm to force the bird to adopt a similar head position at each entry, although some twisting of the body still occurred. Each bird was provided with a perch on a mass balance (Ohaus Scout Pro) and allowed to acclimate to the chamber for at least one day before experimentation. We used operant conditioning to train the bird to associate activation of filming lights and the experimenter placing the feeder in the chamber with the start of feeding bouts. To minimise the ON duration of the four 500W halogen bulbs, we required feeding to begin within 30 s, or the session was skipped (rare among well-trained birds). In general, filming time was <30 s, and the feeder was immediately removed. Body weight during the bout was recorded as the average of pre- and post-feeding measurements. This filming period is shorter than the length of time for a hummingbird feeding to satiation, so we immediately inspected the filming, repeating the session if required; otherwise, the bird was allowed to feed until it returned to the perch, when the feeder was removed again. In addition, after every three trials the bird was allowed to feed ad libitum for 15 minutes, resulting in a half-hour break.

Hummingbirds were recorded flying either with unconstrained postures (unchallenged ‘typical’ wing morphology), or while challenged to hoverfeed in front of a barrier placed around the mouth of the

feeder ('visual mask') or while performing submaximum load lifting. When hover-feeding near a visual obstacle, such as a large flower or this mask, hummingbirds avoid wing collisions with the obstacle by greatly reducing stroke amplitude and increasing stroke frequency and stroke plane angle (Wells, 1993). We constructed a thin plastic mask with the majority of the interior cut out. The side length of the mask was 5.75 cm, about 55% of the wingspan. The remaining thin border was nearly parallel with the wing direction of motion, so we expected minimal aerodynamic interference, in contrast to, for example, a large flower. We did not observe any collision between the wing and the mask. Feeding duration was reduced compared to hovering at the unmasked feeder, and consisted of briefly darting into the feeder, sometimes with their necks extended, with flights lasting a few seconds compared to 10 seconds or longer during the other trials. We also challenged birds through submaximum load lifting trials (Mahalingam and Welch, 2013; Wells, 1993), because aerial agility in hummingbirds is strongly correlated with the capacity to generate large sustained and burst forces (Altshuler et al., 2010a; Segre et al., 2015; Sholtis et al., 2015). Birds were fitted with beads on an elastic band looped around the neck, equal to 20-25% of body weight, depending on the birds' cooperation and any evidence of flight distress. One individual refused to hover normally with any added weight.

Kinematics and mesh construction

We define the wing in terms of the azimuthal position φ, elevation δ, and the geometric angle α of the least squares plane passing through the centroid of the labelled set. The angles φ and δ are reported with respect to the horizontal plane of the lab reference frame, whereas α is given with respect to the vertical. Stroke reversal timings and duration were determined from the position peaks and were used to find the stroke frequency. We constructed a mesh representation of the wing from the labelled points by interpolating forty points along the leading and trailing edges of the mid-downstroke pose, joining spanwise paired points to construct the chord elements (Song et al., 2014). Internal points were spaced at approximately 0.5 mm and connected through Delaunay triangulation, pruning faces with centroids outside the wing perimeter (2D mesh). We then used the custom Matlab function *gridfit* (D'Errico, 2017) to find a mesh scheme fit to the internal wing markers and with a smooth gradient in all directions. To obtain a consistent 3D mesh, we selected the mid-downstroke as the template frame and then projected it onto the mesh at each time step using the *iso2mesh* Matlab toolbox (Tran et al., 2020). In general, the resulting meshes fit the data well although we visually noted some oversmoothing of real, high-curvature features of the secondary flight feathers during the upstroke.

We calculated morphological descriptors of the wing based on the fitted mesh. The wing twist was calculated from the tip and root α as $\Theta=\alpha_{tip}-\alpha_{root}$ [(Leishman, 2000); see (Ingersoll et al., 2018) for a definition based on the average twist rate]. The chordwise camber was determined by h_{chord}/c, where h_{chord}

is the maximum height of the chordwise strip above the chord vector of length *c* (Ennos, 1988). Similarly, we computed a 2D line connecting the wing tip to a point lying at 0.05*c* behind the shoulder. Projecting this line onto the 3D mesh yielded the wing length *R* and mesh height h_{span}, and we express spanwise camber as h_{span}/R. Wing area was determined as the surface area of the mesh. The second moment of area (e.g., (Ellington, 1984a; Kruyt et al., 2014)) was determined from the 2D triangulated mesh. Area moments of posed specimens are often calculated through the product of a section blade radius and chord width (Ellington, 1984a; Kruyt et al., 2014), but because the mesh has area elements *dA*, we quantify the squared second moment of area at every time slice by $\hat{r}^2(S) = \iint_R r^2 dA \,/\, SR^2$, where *r*, *R*, and *S* are respectively the radius of each element from the wing base, the wing length as above, and the 3D mesh area.

Decomposition of shape variation

A data-driven description of wing shape can be found by solving for vectors that span the principal sources of variation in the correlated marker motions. The (economy-size) singular value decomposition of a data matrix $X \in \mathbb{R}^{t\times 3k}$, with *t* time slices and *k* three-dimensional markers, is,

$$X_m = U D_m V^T \qquad \text{eq 2}$$

where the columns of $UD_m \in \mathbb{R}^{t\times 3k}$ are the projection onto the new basis formed by the columns of $V \in \mathbb{R}^{3k\times 3k}$. (Decomposing the transposed data matrix X^T exchanges the senses of *U* and *V*, as for example in (Riskin et al., 2008).) The proportion of variance explained by each of the ranked singular values $d \in D$ is given by $d^2 / \sum d^2$. The variation represented in the *m*th column of UD_m (i.e., the *m*th kinematic mode or shape variable) can be determined by zeroing out all but the *m*th singular value. The interpretation of *V* in terms of kinematic or morphological patterns depends on any processing of the marker data matrix, such as centering or differencing (Bozkurttas et al., 2009; Riskin et al., 2008). We applied eq 2 to shoulder-centered [similar to (Riskin et al., 2008) but without body angle correction] and displacement [ΔX; (Bozkurttas et al., 2009)] coordinates to compare insights from the kinematic modes and shape variables.

Our primary goal was to distinguish morphological from kinematic variation. Let ρ (similarity metric) be the distance between any pair of wing shapes *z* after registering their centered and scaled marker configurations x (Dryden and Mardia, 2016; Slice, 2001),

$$\rho(z_1, z_2) = \min_{\Gamma \in SO(3)} d(x_1\Gamma, x_2) \qquad \text{eq 3}$$

Minimizing over rotations Γ induces a curved shape space (so-called Procrustes analysis, (Dryden and Mardia, 2016; Kendall, 1984; Slice, 2001)), and so some coordinate linearisation is necessary to apply eq

2. Here, we use an orthogonal projection into the linear subspace tangent to the mean configuration [a function of the inverse exponential map; (Dryden and Mardia, 2016; Schlager, 2017; Slice, 2001)], yielding tangent plane coordinates T_pX. We refer to UD_m and V resulting from this pre-processing as the shape scores and shape variables. The scores relate the instantaneous configuration to the roughly planar mean configuration, and so we describe the resulting components as in- and out-of-plane deformations where appropriate. Procrustes analyses were implemented through the R package *Morpho* (Schlager, 2017; Slice, 2001) and we used custom Matlab scripts to find the frequencies of peak power/frequency.

As noted above, some hummingbirds did not sustain hovering in every condition, which would result in unequal shape variances and potentially distort the recovered modes and shape variables between individuals. We therefore performed decompositions for each bird individually using data from the typical hoverfeeding trials, and then projected wing configurations in each treatment onto this basis. The shape variation is therefore in terms of the original, unchallenged flight configurations. Additionally, we used the shape variables during unchallenged flight to assess whether the marker density was sufficient for capturing the complexity of the wing stroke. Watanabe proposed to generate marker sampling curves by comparing the sums of squares obtained by fitting subsets of markers to the complete set (Watanabe, 2018). With sufficient marker density, we expect the sampling curve to plateau, implying that little or no new shape information is gained by adding more markers.

Statistical analyses

We first assessed the temporal correspondence between shape variables and morphological parameters through cross-correlation functions of their respective time series. This analysis reveals the phase relationships between shape variables and morphology. We then applied linear models to predict shape variables from morphology. All measurements were standardised so that the effect of the coefficients was interpretable on the same scale (β). For this regression analysis, we did not include temporal autocorrelations, as our goal was to model how the scores depended on the instantaneous rather than time-lagged morphology. Responses were modelled with respect to wing azimuthal position and elevation, wing twist, area, r□(S), and the chord- and span-wise cambers. We included per-bird random slopes to account for potential inconsistencies in the relationships among birds with differing marking schemes or interindividual variation in morphing patterns. All models were fit in the R package *brms*, with four chains of 2000 iterations each and flat priors for all coefficients. We calculated Bayesian model R^2 as a measure of the model goodness of fit (Bürkner, 2017; Gelman et al., 2019).

Variation in flight behaviour could ostensibly arise through wing shape changes at any interval of the stroke cycle. To compare stroke intervals with shape changes across behaviours and individuals, we

normalised the stroke cycle to unit duration, resulting in two or three repeated measures (tracked stroke cycles) for each bird in each treatment. We used statistical splines to construct a population reference smooth function that captured the temporal variation in the shape scores during typical hoverfeeding flights [mgcv: (Wood, 2017); p-spline with adaptive and cubic cyclic basis). Differences between treatments were then examined through parametric and non-parametric terms. The parametric term encapsulated average differences over the entire stroke cycle. The non-parametric term identified specific temporal intervals where shape scores in each treatment differed from the reference configuration (smooth difference spline, Δsmooth; p-spline with cubic cyclic basis). Additionally, we incorporate random wiggliness in the smooth functions due to interindividual variation using factor-smooths with continuous first derivatives (Wood, 2017). Unlike in the regression analysis, we accounted for autocorrelation because we seek to identify population differences between behaviours, and the shape score at any temporal interval will depend on the stroke cycle history (i.e., the lagged scores). The autocorrelation coefficient for each shape variable was determined by the value that minimised Akaike's information criterion (0.95, 0.94, 0.91, and 0.88 on the first to fourth shape variables, respectively). All analyses were fit through restricted maximum likelihood implemented in the R package *mgcv* (Wood, 2017) and smoothed estimates and confidence intervals were constructed with the package *gratia* (Simpson, 2023). The average fits for each treatment were obtained by adding the Δsmooths to the reference function and zeroing out the factor-smooths.

Wing anatomy

We dissected the left wing of a male Anna's hummingbird (*Calypte anna*) euthanised in an unrelated experiment. The musculoskeletal system and feather insertions were exposed and photographed in a spread posture on a custom light table. Positions of the bones, feathers, and connective tissue between the feathers were traced in Adobe Illustrator. The anatomy was verified in two additional dissections.

RESULTS

The hummingbird wing consists of four feather groups identifiable by common actuation elements (Figure 1A). Our analysis of the anatomy suggests that the primary (P) flight feathers are actuated by either the carpometacarpus (P1-P6), or the first (P7-P9) and second (P10) phalanges of digit II. The secondary (S) flight feathers are actuated by the ulna. The chain of joint motions will therefore result in the largest rotations at the wing tip. We initially decomposed the marker trajectories centered on the mean shoulder position to view the overall path over time (Figure 1B), as has been done previously (Bozkurttas et al., 2009; Riskin et al., 2008). The first mode of the marker trajectories points along the

stroke plane with consistent trajectories for all markers across the wing. The second and third mode appear to incorporate more spatial variation in marker trajectories, as for example, differentiation between the trajectories of primary and secondary flight feathers on the second mode. Clearly, there is a large kinematic contribution to the modes, which obscures the determination of shape changes. We therefore examined the marker trajectories within the reference frame formed by scaling and aligning all markers within individuals (Figure 1C, trajectories with respect to the wing centroid). The resulting deformation trajectories have recognizable components, such as twisting, cambering, and the spreading of the feathers during the downstroke and their partial folding during the upstroke (Maeda et al., 2017).

Wing morphology across the stroke cycle and among behaviours

Hummingbird wings are highly dynamic during hoverfeeding (Figure 1C, Figure 2, Table 1, S1-S4 Videos). The surface area rapidly increases at the start of the stroke cycle (pronation) and reaches its maximum during the mid-downstroke (Figure 2A). Due to feather expansion and folding, the second moment of area $r\square(S)$ is greater (more of the wing area is distributed further from the base) during the downstroke (wing expanded) than during the upstroke (partially folded; Figure 2B). Wing twist, a function of the section angles of attack (Figure 2F), was lowest during the downstroke when the wing is most like the posed states applied in blade element modelling (Altshuler et al., 2010a; Kruyt et al., 2014; Skandalis et al., 2017). The twist minima do not coincide with our placement of stroke reversals based on the wing azimuthal position, although we note that some studies have demarked stroke reversals by the thinnest wing profile when viewed from a vertical position, corresponding to minimum twist [e.g., (Altshuler et al., 2010a)]. The camber profile across the wing is complex (Figure 2G), but greatest during the mid-downstroke. In the mid-downstroke, the wing twists in the direction of feather reinforcement, resulting in a smooth profile. During the upstroke, it appears that the ulna cannot rotate sufficiently to maintain surface contiguity, which opens a gap between the primary and secondary feathers, as noted previously (Maeda et al., 2017). During the upstroke, the twist also acts against the natural camber of the primary feathers, resulting in a flatter distal wing profile. At the wing base, the high camber reflects the dorsal wing surface rather than the thickness profile of the wing section, and we therefore take the midspan camber profile as representative for further analyses.

Hummingbirds substantially alter kinematics when hoverfeeding in front of a visual mask or during submaximum load lifting (Mahalingam and Welch, 2013; Wells, 1993). Stroke amplitude was increased during submaximum load lifting, whereas it decreased at the visual mask. Simultaneously, maximum wing area was increased in front of the visual mask during each of the mid-half strokes (downstroke and upstroke; Figure 2A). During submaximum load lifting, the wing area profile was similar but with greater maximum area in both half-strokes. The distribution of area $r\square(S)$ likewise

differed in terms of timing and the amplitudes of identifiable peaks. Among the most notable differences were the twist and camber profiles at the mask. At the visual mask, wing twist during both halfstrokes was substantially reduced, resulting from distal wing sections being much more inclined relative to the horizontal plane (not necessarily to the stroke plane). In contrast, during submaximum load lifting the twist profile was similar to typical hoverfeeding but at a lower wing angle (Figure 2D). In some individuals, camber appeared to be slightly greater during both half-strokes whereas during submaximum load lifting the camber profile did not greatly differ.

Decomposition of wing dynamic morphology

The morphological variables highlight difficulties comparing wing shape between behaviours. Area changes across the whole wing, but so does the distribution of area with respect to the base. Many morphological parameters involve explicit choices. For example, we summarised the wing sectional angles through the twist (wing tip to base) and the camber at the midspan, but the spatial profiles of each could be highly relevant for describing variation within the stroke cycle and between behaviours. We summarised kinematic and morphological parameters at identified slices of the stroke cycle (Table 1), but this approach could miss important intervals for modulation. To compare among behaviours, we therefore used a data-driven approach to reduce the shape dimensionality and uncover shape variables that capture the full range of variation in hummingbird wing deformations. For each individual, about 80% of the total shape variance was recovered by just 20 markers, whereas 95% recovery was achieved with 40-50 markers (Figure 3A). The subsampling functions were asymptotic, suggesting that notwithstanding interindividual differences in marker number and placement, we could consistently capture the stroke cycle range of shape morphological variation within each individual. We found that the shape variables, ordered by their singular values, corresponded to pairs of dominant temporal frequencies (frequency of the peak power/frequency in Figure 3B). This was most evident in two individuals, in which at least the first 10 shape variables occurred in frequency pairs; the addition of two more cameras for these individuals may have improved our power to identify the dominant frequency in low-variance shape variables. Nonetheless, because the frequency relationships of the first four shape variables were consistent across individuals (Figure 3B), we focus on examining trends in these four variables, which respectively explained ~82%, 10%, 3%, and 1.5% of shape variation. In comparison, proper orthogonal decomposition (POD, Figure 3B), using shoulder-centric or displacement coordinates explained relatively less variance on the first mode (~65-75%), but proportionately greater variance on the second and third modes. The frequency decomposition was less clear in the POD approaches.

Visual examination of the shape variables revealed that the shape variable frequency pairs corresponded to out-of-plane (first and third shape variables) and in-plane (second and fourth)

deformations at each frequency. The mean wing geometry (black dots) for a representative individual is plotted together with the vectors of the linear marker trajectory represented by that shape variable (vector length doubled; Figure 4). The mean wing configuration occurs when the shape scores are zero (Figure 4, right), so the magnitude of the shape score is interpreted as changes in the wing geometry along the directions indicated by the signs of the vectors on each marker. The spatial pattern of deformations on the first shape variable along with the highly consistent shape scores among individuals points to variation linked to twisting in phase with the mid-strokes (mid-downstroke and mid-upstroke). In contrast, scores on the second shape variable, representing in-plane deformations, rapidly increased from negative to positive through the downstroke and stayed elevated during supination and the early upstroke, after which they fell again to negative values. This suggests the second shape variable particularly captures the folding and unfolding of the wing during reversals. The third and fourth shape variables complemented the deformations represented in the first two, at twice the frequency. The third shape variable contrasted out-of-plane deformations that were most distinct during supination and the midstroke poses. The fourth shape variable contrasted in-plane deformations that were most distinct in the early and late downstroke, and in the early upstroke. Scores in the upstroke were less consistent, possibly because of a greater influence on low-variance components of individual variation in wing morphing patterns and in marking scheme (which we cannot distinguish here). It is noteworthy that the third and fourth shape variables were typically zero during pronation and supination, respectively. Thus, after removing the largest kinematic influences, we can interpret the shape variables as contrasts between the sources of in- and out-of-plane at identifiable intervals of the stroke cycle.

Comparison of shape variables to kinematics and morphology

We next sought to study whether the shape changes identified through decomposition of marker trajectories could be explained in specific terms through widely used morphological descriptors. We first examined the cross-correlation of each shape variable and key kinematic and morphological parameters. The first shape variable was a quarter cycle out of phase with the azimuthal wing position, whereas the second shape variable was in phase (Figure 5). The third and fourth shape variables were better associated with wing elevation, which is similarly twice the stroke frequency for a typical J-shaped wing tip path (Figure 2B). Wing twist was the sole parameter to be strongly linearly correlated with a shape variable (Figure 5). The other variables exhibited complex periodicity. Taking the lag into account through cross-correlation analysis, wing area and chordwise camber were the best correlated with the second shape variable. Spanwise camber appeared weakly related to the third shape variable, whereas there were no obvious trends between the fourth shape parameter and any morphological parameter.

We next used multiple regression model to identify how the instantaneous value in each shape parameter depended on the instantaneous morphological parameters. We included kinematic parameters to account for mutual associations with the periodicity of the signals rather than any direct relationships between the shape and morphology. The first shape variable was nearly solely explained by variation in wing twist (normalised regression weights β in Figure 6), which reinforced our visual interpretation of the role of twist based on the marker motions (Figure 4). Moreover, the model R^2 (morphology together with kinematics) of the first shape variable was close to unity. Unlike the first shape variable, none of the other shape variables can be considered simple linear functions of morphological parameters, because none were correlated with near-zero phase (Figure 4). The second shape variable, representing in-plane deformations, was best associated with temporal trends in area, even though the dynamics of the respective variables differ, especially during reversals (compare to Figure 2). The third and fourth shape variables were less well explained, with model $R^2 \sim 0.64$ and 0.36, respectively. All morphological parameters other than $r\square(S)$ were associated with variation in the third shape variable, although excepting spanwise camber, each had wide credible intervals spanning near zero. The sole parameter associated with the fourth shape variable was $r\square(S)$. These results suggest that twist and area changes are the major parameters associated with the dominant sources of in- and out-of-plane deformations during reversals and mid-strokes, respectively. In contrast, the spanwise camber and $r\square(S)$ appear to correspond to higher frequency components of dynamic shape changes, though caution is needed because of the nonlinearity of the relationships and the overall low model R^2.

Spatiotemporal variation in wing shape among hoverfeeding behaviours

Flying animals, particularly vertebrates, possess enormous degrees of freedom for controlling wing motions to support diverse flight behaviours. Modulation may occur during subintervals of the stroke cycle, and so selecting time slice at which to compare wing morphology, such as during the mid-strokes or during reversals (Table 1), may reduce our power to detect real differences in flight behaviour. We therefore adopted an approach based on statistical splines (Wood, 2017) to statistically identify temporal intervals with wing shape changes. The population average of each shape variable was captured in a reference smooth, representing typical shape dynamics during unchallenged hoverfeeding (Figure 7). In our models, individual random variation was captured through factor-smooths (i.e., a random effect of functions), which were generally evenly distributed around zero over the course of the stroke cycle, suggesting there was no systematic underfitting of the population model at any point. Differences in wing shape were determined by parametric and non-parametric (Δsmooth) functions, respectively identifying average differences over the entire stroke cycle and differences at specific subintervals.

Hoverfeeding in front of the visual mask and during submaximum load lifting entailed significant changes in wing shape across the stroke cycle (Figure 7). In front of the visual mask, the first shape variable suggests a reduced wing twist (shape score closer to zero) during the late downstroke and mid-upstroke, and greater twist during the mid-upstroke. Prominent peaks and valleys in the second shape variable appear to point to widespread changes in shape coinciding with the mid-half strokes and reversals. There was an identifiable parametric increase in scores on the second shape variable, suggesting a small increase in wing area throughout the stroke cycle. The most dramatic changes in shape scores were on the third shape variable, in which a large dip during the upstroke effectively offset the peak during the same phase of typical hoverfeeding. The most identifiable difference on the fourth shape variable was during pronation. The pattern of shape changes during submaximum load lifting particularly suggests a role for the late downstroke and modulation of the entire upstroke. Scores on the first and third shape variables did not greatly differ from typical hoverfeeding except for the early upstroke and a large interval encompassing the late upstroke and pronation. Conversely, the second and fourth shape variables suggest widespread and prominent changes in area dynamics during the late downstroke and throughout the upstroke implied by the changes in area and $r_{\square}(S)$ (Figure 2). In real terms, these analyses suggest that both in- and out-of-plane wing deformations are spatially and temporally widespread while hoverfeeding in front of the visual mask, whereas submaximum load lifting appear to be most associated with in-plane deformations, particularly during the latter downstroke and throughout the upstroke. Importantly, quantifying dynamical changes among behaviours requires considering not just the first shape variable that explains the majority of shape variation. The lower shape variables identify modality-specific deformation patterns despite explaining <10% of variation each, demonstrating that explained variance (i.e., ranking the squared singular values) is insufficient for predicting behavioural plasticity.

DISCUSSION

Complex deformation dynamics may be critical to soft tissues' function, and in flying vertebrates they are central to behavioural and locomotor plasticity. The importance of deformations is at odds with morphological descriptors derived primarily from posed specimens and fixed-wing and rotary-blade aircraft. It seems natural to distinguish between kinematics and morphology as the components of performance respectively measurable during or independently of behaviour (Ellington, 1984a; Ellington, 1984b). However, even in insects that lack active morphing, it is clear that the wing morphology has evolved to support deformations as critical elements of performance (Lehmann et al., 2011; Lucas et al., 2014; Mountcastle and Combes, 2013; Young et al., 2009; Zheng et al., 2013). Because the bending and twisting is so crucial to performance (Lehmann et al., 2011; Zheng et al., 2013), ecological or

evolutionary inference based on the planform shape alone is necessarily limited. In general, increasingly granular analyses blur the distinction between morphology and kinematics because the entire body is in motion. We approached the dichotomization by considering wing shape as the information left over after rotating all wing poses into a common reference frame. This approach is possible because we distinguish between the body and wing as separate body parts, which is generally reasonable in insects and birds, but is less clearly distinguished in animals like bats, some fish fins, or in squid (Bartol et al., 2018; Bozkurttas et al., 2009; Riskin et al., 2012). By rotating and scaling all wing configurations into a common reference frame, our linear decomposition yields vectors spanning the axes of the periodic marker trajectories around the mean marker position (Figure 1). These axes explain successively smaller elements of the periodicity, resulting in a frequency decomposition of the in- and out-of-plane wing motions. Moreover, within each component, the shape scores contrast recognisable subintervals of the stroke cycle, like the midstrokes and the reversals (Figures 4,7).

Hummingbirds naturally vary among individuals and species in wing shape and dimensions (Kruyt et al., 2014; Skandalis et al., 2017; Tobalske et al., 2007), but the extent to which wing morphing and shape changes are related to specific behaviours and agility has been less clear. Modal decompositions have been used to find low-rank representations of shape and thus reduce the number of comparisons (Bartol et al., 2018). Nonetheless, it has been difficult to interpret such modes in any specific terms or to choose the dimensionality of the reduced rank representation except by the fraction of explained variance. Our method provided a principled method for selecting four shape variables, comprising the in- and out-of-plane components of deformations at the first two integer multiple of the stroke frequency (higher multiples had higher population uncertainty, Figure 3). We found that twisting dominates hummingbird shape changes throughout the stroke cycle, as a proportion of quantified shape variance. In turn, we observed substantial changes in the twist profile while hoverfeeding in front of the visual mask throughout the stroke cycle and during submaximum load lifting principally during the upstroke. The prominence of twisting in the typical stroke cycle follows from crown hummingbirds' morphological innovations that enabled supination and weight support during the upstroke (Hedrick et al., 2011; Warrick et al., 2005). Wing area changes formed the second largest component of shape variation. Hoverfeeding in both challenges was associated with differences in maximum wing area and the area dynamics (Figures 2, 7). Notably, dramatic differences in wing shape while hoverfeeding in front of the visual mask or during submaximum load lifting were represented on the third and fourth shape variables respectively, even though each explained <5% of shape variance in typical flight. On this basis, we believe it is prudent to deemphasise explained variance as a measure of importance in modal analyses. Although the first shape variable explains ~80% of population shape variance, most individual time slices roughly correspond to wing configurations during the translatory stroke phase. This is because stroke

reversals are rapid events represented by few individual time slices, and thus represent a smaller partition of the population shape variance. However, stroke reversals are critical for aerodynamic force production in reciprocating wings (Dickinson et al., 1999; Ravi et al., 2020; Song et al., 2015) and so changes in wing shape during these periods are likely to be crucial as well. Indeed, the predominance of transients in fluidic propulsion suggests that even brief changes at a certain interval may have magnified importance in terms of life-time performance. Our results suggest that distinct behaviours are associated with shape changes at distinct subintervals of the stroke cycle.

Understanding the functional relevance of hummingbird wing morphing will require further detailed studies of forces. Hummingbird shape deformations arise through fluid-structure interactions and active muscular control. We could not address the aerodynamic forces contributing to or that develop as a consequence of these shape changes, for example the changes in wing tip angle with respect to flow (Lucas et al., 2014). Power muscle activity (pectoralis major and supracoracoideus) has been well-studied [e.g., (Altshuler et al., 2010b; Konow et al., 2017; Mahalingam and Welch, 2013; Ravi et al., 2020)], but the roles of handwing muscles remain largely enigmatic (Altshuler et al., 2012). Muscular forces may also stiffen to limit the influence of aerodynamic and inertial forces, as in fish bodies (Tytell et al., 2016). For example, handwing muscles may be recruited to act against inertial bending due to the rapid accelerations of the foreshortened stroke cycle in front of the visual mask. An important step will also be to pair deformation studies with the actuating movements [Figure 1; (Hedrick et al., 2011)]. Undoubtedly, a valuable tool going forward will be unbiased (i.e., no marker choices) dense reconstruction of the entire body and wing surface (Cheney et al., 2020). Marking functions as a spatial low-pass filter, which may have further contributed to our limited capacity to resolve higher frequency deformation components in all individuals. In all cases, we believe that we will require conceptual advances in terms of our understanding of the relationships between bodies and their motions to uncover functional and evolutionary principles of soft tissues and their complex dynamics.

ACKNOWLEDGMENTS

We are grateful to Drs. Rajat Mittal, Daniel K. Riskin, and Laurent Younes for insightful discussions on flapping aerodynamics and quantifying dynamical shape variation. This work was supported by a Natural Sciences and Engineering Research Council of Canada Postgraduate Scholarship (to DAS) and Discovery Grant (to DLA, RGPIN-2016-05381), and by the US Air Force Office of Scientific Research (grant number FA9550-16-1-0182, monitored by Dr B.L. Lee).

Table 1 Kinematic and morphological variation among hummingbirds during identified phases of three flight conditions. Values are presented as means and 95% confidence intervals for the number of individuals (N) in each condition. Number of individuals, N. Midspan section angle relative to vertical, α. First moment of area, $r\square(S)$.

Stroke phase	Condition	N	Position (°)	Elevation (°)	α (°)	Length (cm)	Area (cm^2)	$r\square(S)$	Twist (°)	Chordwise camber (%)	Spanwise camber (%)
Pronation	Visual mask	4	49.12 (5.697)	19.347 (3.854)	76.422 (2.846)	4.722 (0.04)	5.455 (0.147)	0.487 (0.004)	4.58 (3.597)	5.248 (0.718)	6.455 (0.637)
	Typical flight	5	28.388 (7.415)	22.239 (2.392)	83.548 (1.917)	4.749 (0.048)	5.47 (0.12)	0.485 (0.003)	7.472 (2.781)	4.321 (0.731)	6.954 (0.719)
	Submaximum load lifting	3	24.881 (10.332)	23.123 (2.031)	84.26 (1.834)	4.752 (0.012)	5.452 (0.069)	0.485 (0.003)	6.485 (3.534)	5.18 (0.62)	7.123 (1.096)
Mid-downstroke			93.185 (5.5)	9.439 (5.566)	29.593 (3.014)	4.96 (0.062)	6.414 (0.188)	0.499 (0.003)	-36.98 (2.656)	10.048 (0.447)	7.391 (0.697)
			91.276 (5.475)	7.392 (2.318)	20.719 (2.275)	5.001 (0.039)	6.388 (0.106)	0.496 (0.003)	-35.456 (1.665)	12.033 (0.43)	6.033 (0.565)
			98.195 (8.605)	12.79 (1.261)	19.866 (3.813)	5.031 (0.015)	6.5 (0.054)	0.497 (0.004)	-34.942 (3.907)	12.537 (0.253)	7.837 (0.624)
Supination			131.825 (4.284)	2.994 (6.401)	74.789 (2.809)	4.79 (0.038)	5.75 (0.118)	0.486 (0.005)	59.1 (6.204)	5.143 (1.318)	19.9 (0.918)
			157.764 (4.277)	10.934 (1.687)	72.624 (2.25)	4.834 (0.036)	5.877 (0.116)	0.488 (0.004)	45.432 (5.45)	2.712 (0.813)	17.384 (0.766)
			174.845 (4.724)	19.056 (2.596)	73.763 (2.575)	4.849 (0.022)	5.853 (0.074)	0.488 (0.004)	40.246 (6.357)	2.236 (0.787)	15.943 (0.804)
Mid-upstroke			87.858 (5.082)	0.208 (6.431)	56.704 (4.135)	4.709 (0.055)	5.474 (0.133)	0.479 (0.004)	68.806 (5.333)	4.228 (1.004)	14.469 (0.673)
			90.357 (5.863)	2.302 (2.41)	40.584 (2.397)	4.743 (0.046)	5.48 (0.116)	0.479 (0.003)	74.342 (3.72)	4.755 (0.735)	12.845 (0.449)
			95.914 (8.45)	5.794 (2.489)	33.795 (2.888)	4.755 (0.021)	5.455 (0.053)	0.479 (0.003)	76.891 (1.396)	4.622 (0.365)	12.438 (0.655)

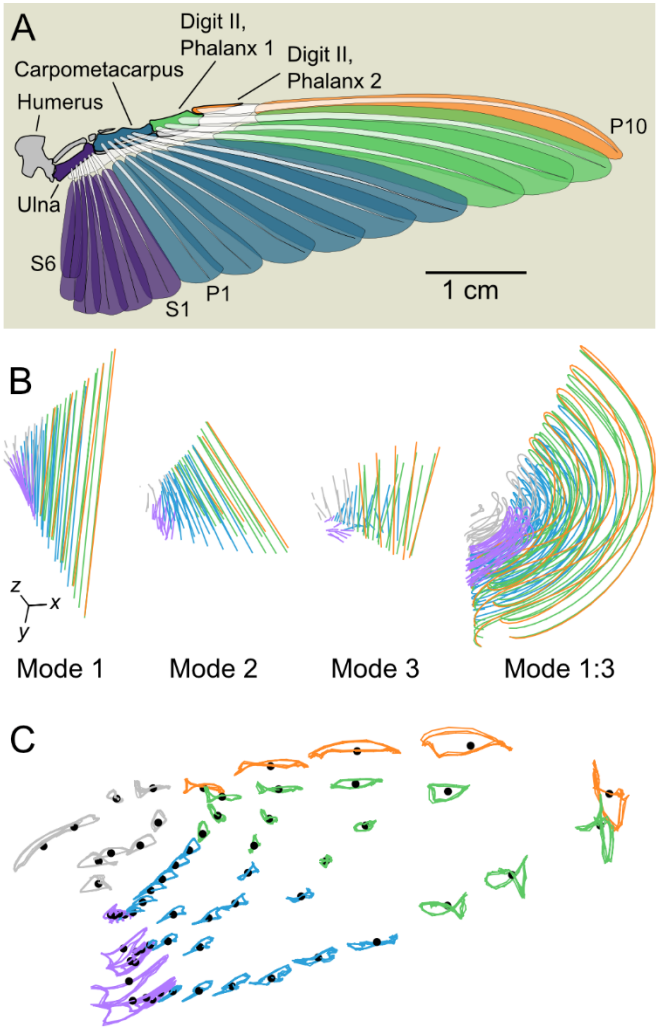

Figure 1 Functional anatomy of the hummingbird wing. **A** The hummingbird handwing is composed of four groups of feathers that insert on and are actuated by the ulna (secondary feathers, S6-S1), the fused carpometacarpus (primary feathers, P1-P6), and the first (P7-P9) and second (P10) phalanges of digit II. **B** The wing undergoes complex deformations during the stroke cycle. The first three kinematic modes (singular value decomposition) reconstruct the basic features of the hummingbird figure-eight stroke cycle. The first mode principally represents marker trajectories through the stroke plane (stroke amplitude). The first mode is oriented primarily along the stroke plane but lower modes also incorporate complex aspects of shape changes, notably differential paths of secondary feathers near the wing base and the distal primaries. **C** We separate kinematics from morphology by registering the marker configurations at every time step to a mean configuration and scaling the marker set to unit size. Trajectories of the marker coordinates in this frame of reference describe major shape changes, like the path of the wing base and tip.

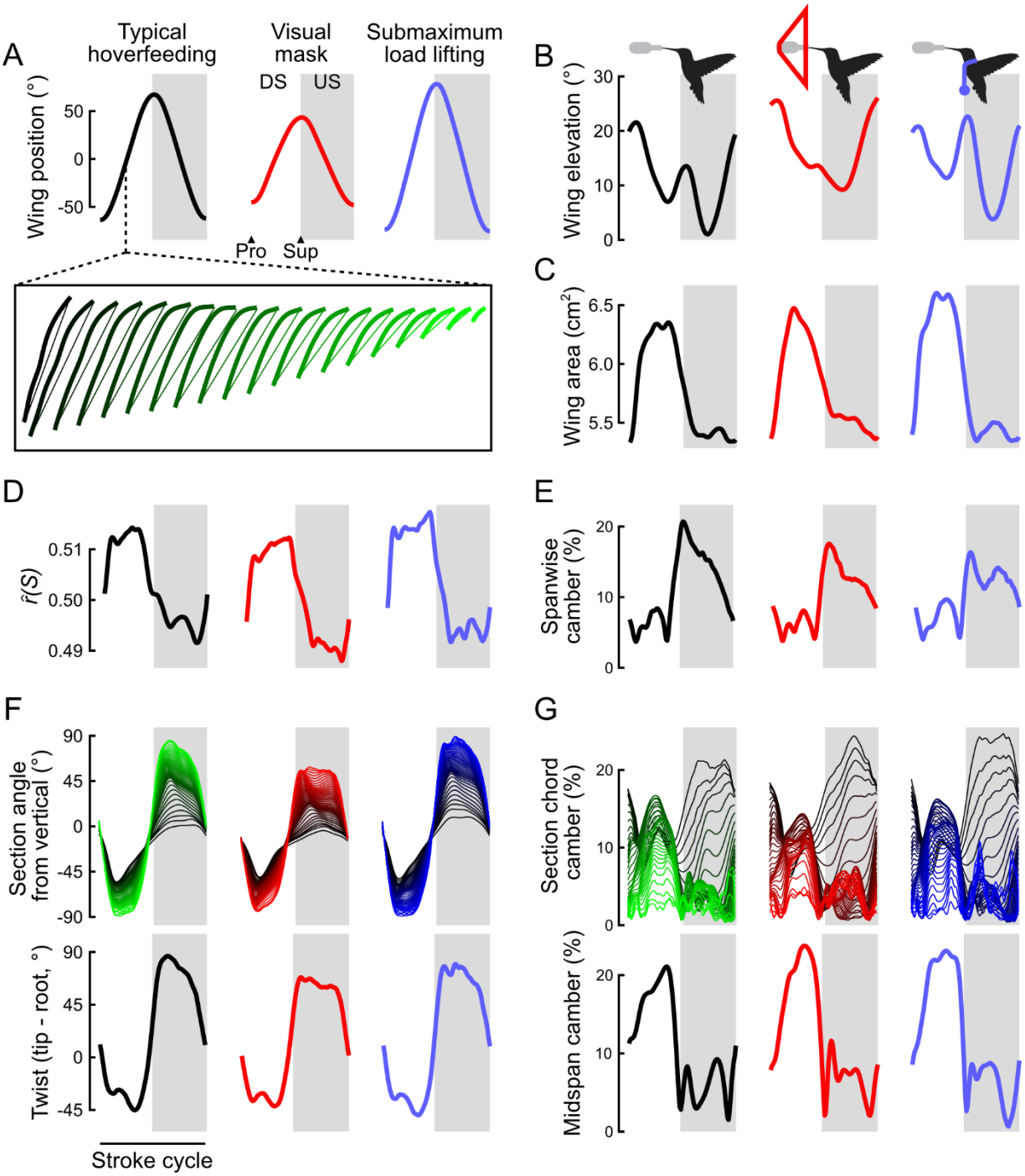

Figure 2 Kinematics and morphology of typical hoverfeeding and hoverfeeding in front of a visual mask or during submaximum load lifting. Each trace is the stroke-averaged response for one individual through downstroke (DS), supination (Sup), upstroke (US), and pronation (Pro). **A-B** Kinematic changes in front of a mask include decreased amplitude and, in this individual, increased stroke elevation, whereas flight during submaximum load lifting involved increased amplitude and a more prominent elevation peak during supination. At each time point, the tracked markers were used to reconstruct the 2D surface

consisting of connected leading- and trailing edge points and the 3D cambered surface. The surface reconstruction was used to quantify morphological parameters including wing area (**C**), spanwise camber (**D**), and second moment of area (**E**), each of which show distinct average time courses in each flight condition. **E-F** The sectional wing angle and camber were used to derive a wing average twist and midspan camber profile, respectively. Twist is greatly reduced in the wing during the upstroke in front of the visual mask, as is the wing camber temporal profile.

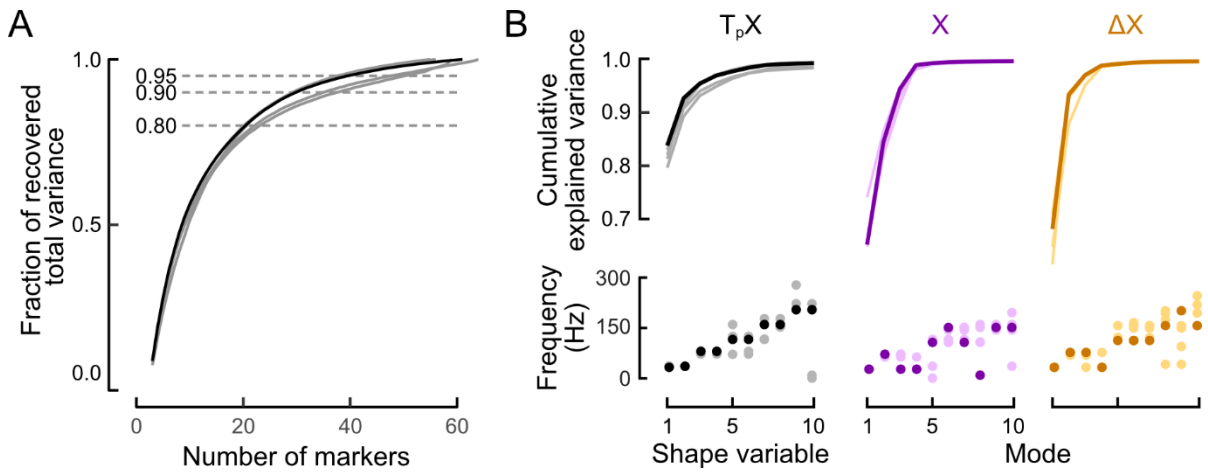

Figure 3 Linear decompositions of wing shape variation. **A** The sufficiency of marker sampling was examined by the fraction of recoverable shape variance in random subsets of markers in tangent coordinates T_pX. The asymptotic sampling trend indicates that little new shape information is gained by adding more markers. **B** Decomposition of T_pX yielded shape variables that efficiently compressed wing shape variation during typical hovering. The first shape variable explained ~80% of shape variance, and the first four explained >95% of variance. The dominant frequency in the scores of each of the first four shape variables occurred in frequency pairs. In comparison, kinematic modes calculated from body-centered (X) or displacement (ΔX) coordinates contained ~70% of variance on one mode but nearly 99% on the first three. The relationships between kinematic modes and their dominant frequencies were less clear. In all plots, each line or circle represents one individual. Dark lines and points correspond to the representative individual in Figure 2.

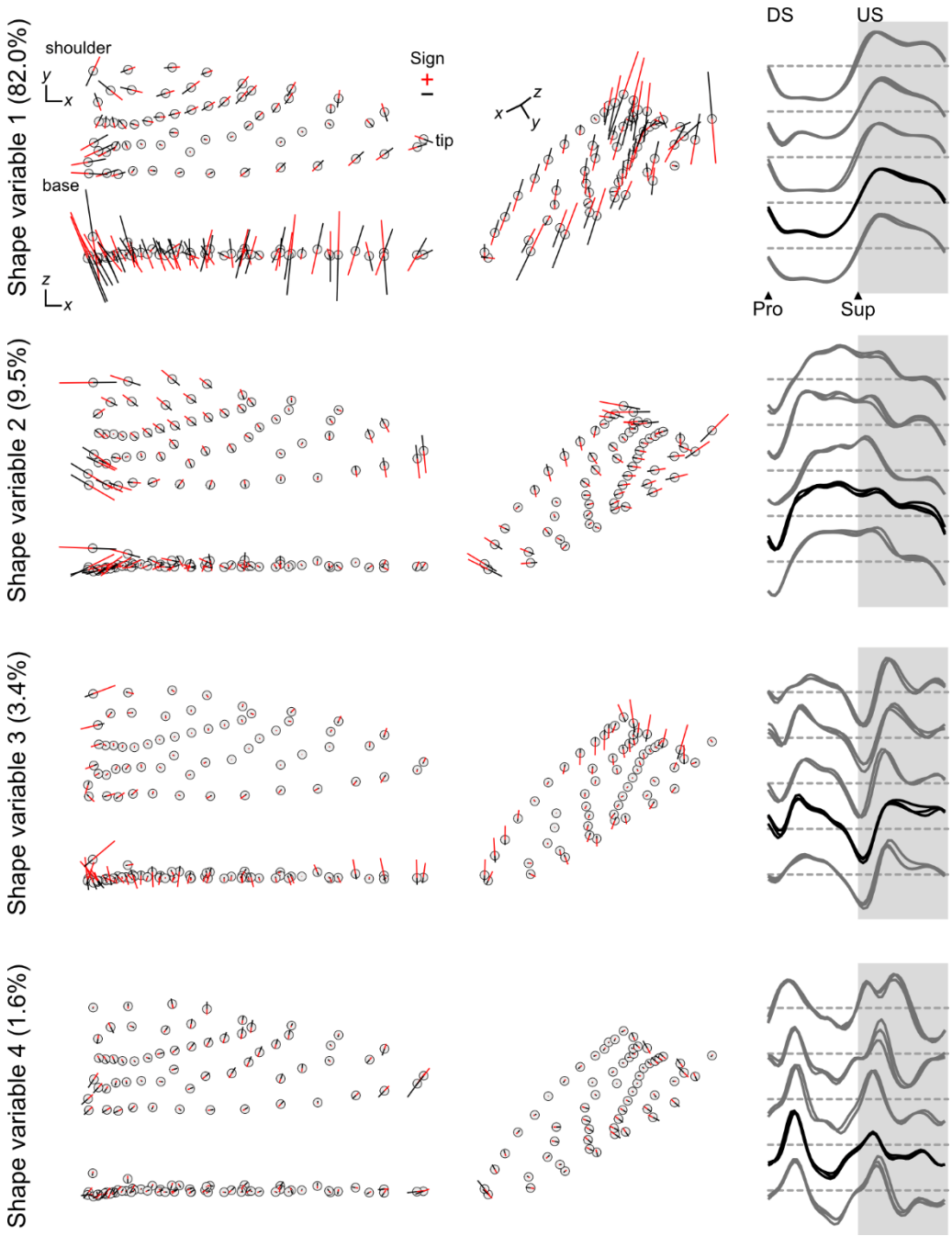

Figure 4 Shape variables capture consistent sources of variation among individuals. The trajectory of each marker (open circle) is represented by red (positive scores) and black (negative scores) lines (scaled to twice the range of variation in this individual). Time traces of normalised individual scores per digitised wingbeat are shown at right (black is the representative individual at left and in Figure 2). The first and third shape variables largely correspond to out-of-plane deformations whereas the second shape variable corresponds to in-plane deformations.

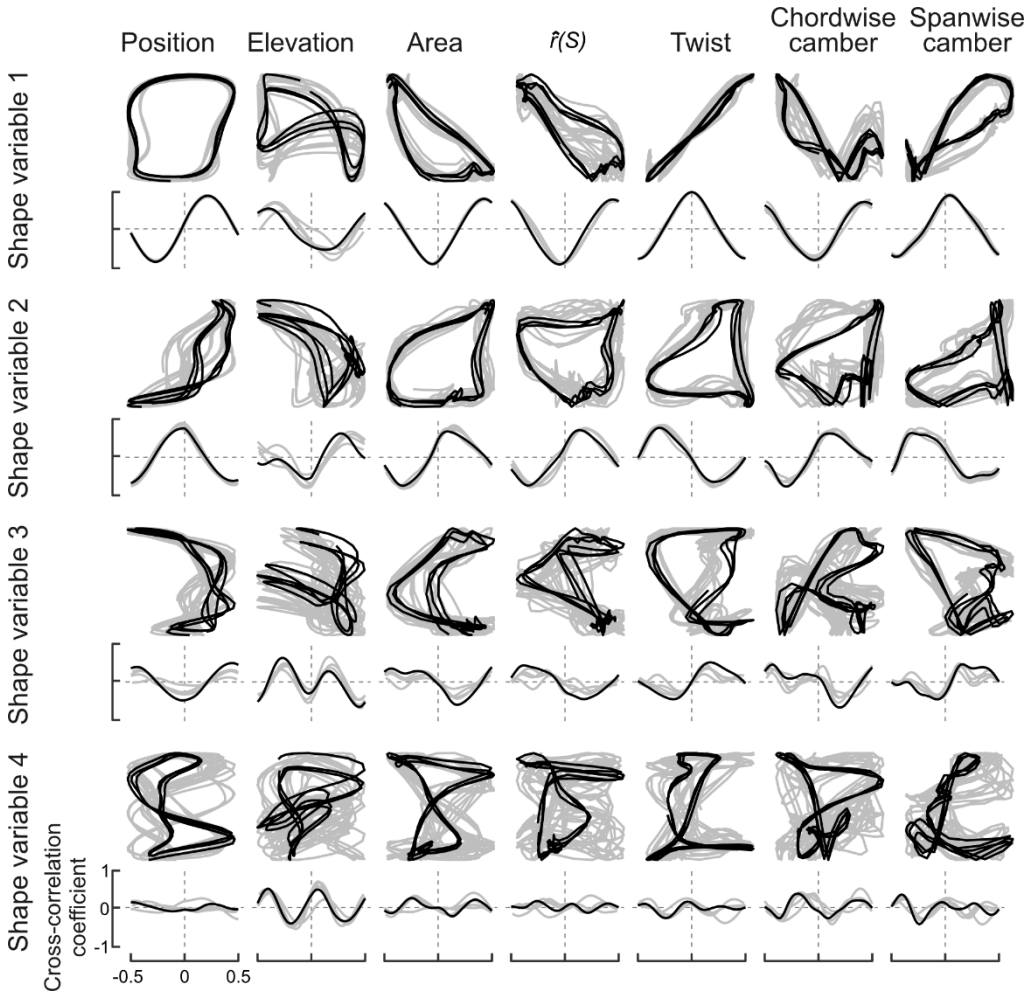

Figure 5 Correlations between shape modes, kinematics, and aerodynamic shape descriptors. The first shape mode is strongly linearly correlated and in phase only with wing twist. The second and third shape components do not exhibit obvious relationships with typical descriptors, although cross-correlation coefficients are high on the second mode. Each line represents one individual through two or three consecutive wing beats, and the black line is the representative individual in Figure 2.

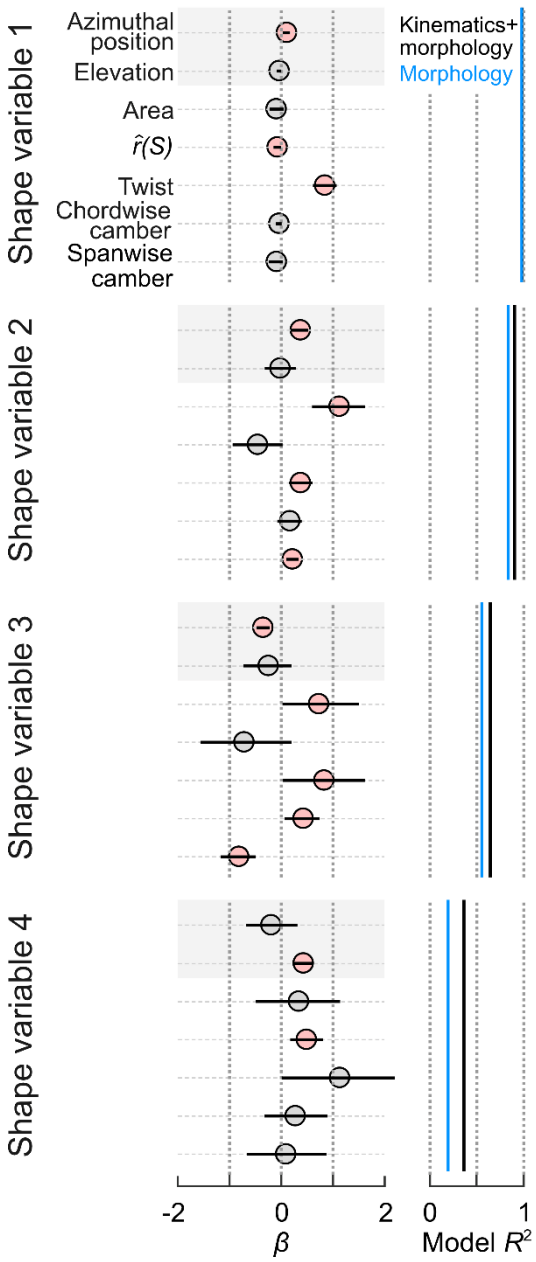

Figure 6 Shape modes correspond to distinct combinations of morphological descriptors. The models for the first two shape variables explained the great majority of the variance in the responses in terms of morphological components (model R^2). Based on the magnitudes of the standardised regression β for each parameter, we interpret the first shape variable as largely representing wing twist and the second shape variable as representing wing area. Variance in the scores of the third and fourth shape variables was not as well explained, but appeared to be particularly associated with spanwise camber and the second moment of area, $r\square(S)$.

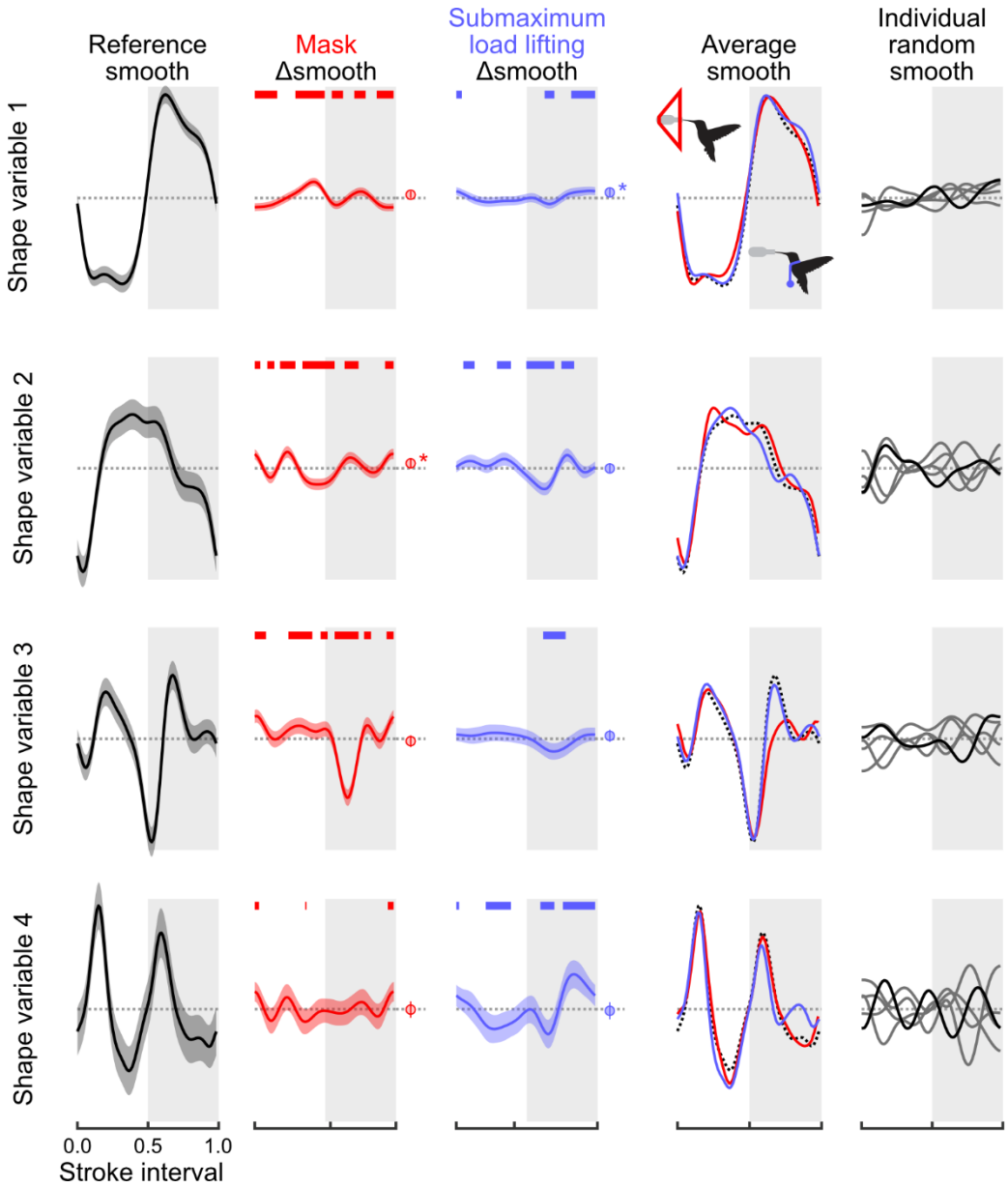

Figure 7 Hoverfeeding in different flight conditions involves changes in wing shape throughout the stroke cycle. The average trend of wing shape scores in typical hoverfeeding on each shape variable was calculated in typical hoverfeeding (reference smooth). We determined a difference smooth (Δsmooth) in each flight challenge (visual mask or submaximum load lifting), representing intervals with significant changes in wing shape. For comparison, a mean function in each challenge is depicted by the sum of the reference and difference functions, and a parametric intercept (not shown). Flying in front of the visual mask entails changes in wing shape in all shape variable at all intervals, whereas the major wing shape changes in submaximum load lifting were encapsulated by the second shape variable. The individual

random smooths (far right), capturing individual variation in marker placement and wing deformations, do not show major trends that would suggest a bias in the reference or Δsmooth functions.

Adams, D. C. and Cerney, M. M. (2007). Quantifying biomechanical motion using Procrustes motion analysis. *Journal of Biomechanics* **40**, 437–444.

Aiello, B. R., Westneat, M. W. and Hale, M. E. (2017). Mechanosensation is evolutionarily tuned to locomotor mechanics. *PNAS* 201616839.

Akanyeti, O., Thornycroft, P. J. M., Lauder, G. V., Yanagitsuru, Y. R., Peterson, A. N. and Liao, J. C. (2016). Fish optimize sensing and respiration during undulatory swimming. *Nat Commun* **7**,.

Altshuler, D. L., Dudley, R., Heredia, S. M. and McGuire, J. A. (2010a). Allometry of hummingbird lifting performance. *J Exp Biol* **213**, 725–734.

Altshuler, D. L., Welch, K. C., Cho, B. H., Welch, D. B., Lin, A. F., Dickson, W. B. and Dickinson, M. H. (2010b). Neuromuscular control of wingbeat kinematics in Anna's hummingbirds (Calypte anna). *Journal of Experimental Biology* **213**, 2507–2514.

Altshuler, D. L., Quicazán-Rubio, E. M., Segre, P. S. and Middleton, K. M. (2012). Wingbeat kinematics and motor control of yaw turns in Anna's hummingbirds (Calypte anna). *Journal of Experimental Biology* **215**, 4070–4084.

Bachmann, T., Emmerlich, J., Baumgartner, W., Schneider, J. M. and Wagner, H. (2012). Flexural stiffness of feather shafts: geometry rules over material properties. *J Exp Biol* **215**, 405–415.

Badger, M. A., Wang, H. and Dudley, R. (2019). Avoiding topsy-turvy: how Anna's hummingbirds (Calypte anna) fly through upward gusts. *Journal of Experimental Biology* **222**, jeb176263.

Baliga, V. B., Szabo, I. and Altshuler, D. L. (2019). Range of motion in the avian wing is strongly associated with flight behavior and body mass. *Science Advances* **5**, eaaw6670.

Bartol, I. K., Krueger, P. S., York, C. A. and Thompson, J. T. (2018). New approaches for assessing squid fin motions: coupling proper orthogonal decomposition with volumetric particle tracking velocimetry. *Journal of Experimental Biology* **221**, jeb176750.

Boerma, D. B., Breuer, K. S., Treskatis, T. L. and Swartz, S. M. (2019). Wings as inertial appendages: how bats recover from aerial stumbles. *Journal of Experimental Biology* **222**, jeb204255.

Bozkurttas, M., Mittal, R., Dong, H., Lauder, G. V. and Madden, P. (2009). Low-dimensional models and performance scaling of a highly deformable fish pectoral fin. *Journal of Fluid Mechanics* **631**, 311–342.

Bürkner, P.-C. (2017). brms: An R package for Bayesian multilevel models using Stan. *Journal of Statistical Software* **80**, 1–28.

Cheney, J. A., Stevenson, J. P. J., Durston, N. E., Song, J., Usherwood, J. R., Bomphrey, R. J. and Windsor, S. P. (2020). Bird wings act as a suspension system that rejects gusts. *Proc. R. Soc. B.* **287**, 20201748.

Cheney, J. A., Rehm, J. C., Swartz, S. M. and Breuer, K. S. (2022). Bats actively modulate membrane compliance to control camber and reduce drag. *Journal of Experimental Biology* **225**, jeb243974.

Deetjen, M. E., Biewener, A. A. and Lentink, D. (2017). High-speed surface reconstruction of a flying bird using structured light. *Journal of Experimental Biology* **220**, 1956–1961.

D'Errico, J. (2017). Surface Fitting using gridfit.

Dickinson, M. H., Lehmann, F.-O. and Sane, S. P. (1999). Wing Rotation and the Aerodynamic Basis of Insect Flight. *Science* **284**, 1954–1960.

Dryden, I. L. and Mardia, K. V. (2016). *Statistical Shape Analysis, with Applications in R*. John Wiley & Sons, Ltd.

Ellington, C. P. (1984a). The aerodynamics of hovering insect flight. II. Morphological parameters. *Phil. Trans. R. Soc. Lond. B* **305**, 17–40.

Ellington, C. P. (1984b). The aerodynamics of hovering insect flight. III. Kinematics. *Phil. Trans. R. Soc. Lond. B* **305**, 41–78.

Ennos, A. R. (1988). The Importance of Torsion in the Design of Insect Wings. *J Exp Biol* **140**, 137–160.

Gelman, A., Goodrich, B., Gabry, J. and Vehtari, A. (2019). R-squared for Bayesian Regression Models. *The American Statistician* **73**, 307–309.

Gillies, J. A., Thomas, A. L. R. and Taylor, G. K. (2011). Soaring and manoeuvring flight of a steppe eagle Aquila nipalensis. *Journal of Avian Biology* **42**, 377–386.

Hedrick, T. L. (2008). Software techniques for two- and three-dimensional kinematic measurements of biological and biomimetic systems. *Bioinspir. Biomim.* **3**, 034001.

Hedrick, T. L., Tobalske, B. W., Ros, I. G., Warrick, D. R. and Biewener, A. A. (2011). Morphological and kinematic basis of the hummingbird flight stroke: scaling of flight muscle transmission ratio. *Proceedings of the Royal Society B: Biological Sciences* **279**, 1986–1992.

Hedrick, T. L., Tobalske, B. W., Ros, I. G., Warrick, D. R. and Biewener, A. A. (2012). Morphological and kinematic basis of the hummingbird flight stroke: scaling of flight muscle transmission ratio. *Proc. R. Soc. B* **279**, 1986–1992.

Heinold, M. and Kähler, C. J. (2015). Wing-Surface Reconstruction of a Lanner-Falcon in Free Flapping Flight with Multiple Cameras. In *Image and Video Technology*, pp. 392–403. Springer, Cham.

Hubel, T. Y., Hristov, N. I., Swartz, S. M. and Breuer, K. S. (2012). Changes in kinematics and aerodynamics over a range of speeds in Tadarida brasiliensis, the Brazilian free-tailed bat. *Journal of The Royal Society Interface* **9**, 1120–1130.

Ingersoll, R., Haizmann, L. and Lentink, D. (2018). Biomechanics of hover performance in Neotropical hummingbirds versus bats. *Science Advances* **4**, eaat2980.

Iriarte-Diaz, J., Riskin, D. K., Breuer, K. S. and Swartz, S. M. (2012). Kinematic Plasticity during Flight in Fruit Bats: Individual Variability in Response to Loading. *PLoS ONE* **7**, e36665.

Kendall, D. G. (1984). Shape Manifolds, Procrustean Metrics, and Complex Projective Spaces. *Bulletin of the London Mathematical Society* **16**, 81–121.

Koehler, C., Liang, Z., Gaston, Z., Wan, H. and Dong, H. (2012). 3D reconstruction and analysis of wing deformation in free-flying dragonflies. *Journal of Experimental Biology* **215**, 3018–3027.

Konow, N., Cheney, J. A., Roberts, T. J., Iriarte-Díaz, J., Breuer, K. S., Waldman, J. R. S. and Swartz, S. M. (2017). Speed-dependent modulation of wing muscle recruitment intensity and kinematics in two bat species. *Journal of Experimental Biology* **220**, 1820–1829.

Kruyt, J. W., Quicazán-Rubio, E. M., Heijst, G. F. van, Altshuler, D. L. and Lentink, D. (2014). Hummingbird wing efficacy depends on aspect ratio and compares with helicopter rotors. *J. R. Soc. Interface* **11**, 20140585.

Le, T. Q., Truong, T. V., Park, S. H., Truong, T. Q., Ko, J. H., Park, H. C. and Byun, D. (2013). Improvement of the aerodynamic performance by wing flexibility and elytra–hind wing interaction of a beetle during forward flight. *J. R. Soc. Interface* **10**,.

Lehmann, F.-O., Gorb, S., Nasir, N. and Schützner, P. (2011). Elastic deformation and energy loss of flapping fly wings. *J. Exp. Biol.* **214**, 2949–2961.

Leishman, J. G. (2000). Principles of Helicopter Aerodynamics. *Cambridge University Press*.

Lockwood, R., Swaddle, J. P. and Rayner, J. M. V. (1998). Avian wingtip shape reconsidered: Wingtip shape indices and morphological adaptations to migration. *Journal of Avian Biology* **29**, 273–292.

Lucas, K. N., Johnson, N., Beaulieu, W. T., Cathcart, E., Tirrell, G., Colin, S. P., Gemmell, B. J., Dabiri, J. O. and Costello, J. H. (2014). Bending rules for animal propulsion. *Nat Commun* **5**, 3293.

Maeda, M., Nakata, T., Kitamura, I., Tanaka, H. and Liu, H. (2017). Quantifying the dynamic wing morphing of hovering hummingbird. *Royal Society Open Science* **4**, 170307.

Mahalingam, S. and Welch, K. C. (2013). Neuromuscular control of hovering wingbeat kinematics in response to distinct flight challenges in the ruby-throated hummingbird, Archilochus colubris. *Journal of Experimental Biology* **216**, 4161–4171.

Matloff, L. Y., Chang, E., Feo, T. J., Jeffries, L., Stowers, A. K., Thomson, C. and Lentink, D. (2020). How flight feathers stick together to form a continuous morphing wing. *Science* **367**, 293–297.

Mountcastle, A. M. and Combes, S. A. (2013). Wing flexibility enhances load-lifting capacity in bumblebees. *Proceedings of the Royal Society B: Biological Sciences* **280**, 20130531–20130531.

Muijres, F. T., Johansson, L. C., Barfield, R., Wolf, M., Spedding, G. R. and Hedenström, A. (2008). Leading-Edge Vortex Improves Lift in Slow-Flying Bats. *Science* **319**, 1250–1253.

Muijres, F. T., Johansson, L. C. and Hedenström, A. (2012). Leading edge vortex in a slow-flying passerine. *Biology Letters* **8**, 554–557.

Norberg, U. M. and Rayner, J. M. V. (1987). Ecological Morphology and Flight in Bats (Mammalia; Chiroptera): Wing Adaptations, Flight Performance, Foraging Strategy and Echolocation. *Philosophical Transactions of the Royal Society of London. Series B, Biological Sciences* **316**, 335–427.

Phan, H. V., Truong, Q. T. and Park, H. C. (2017). An experimental comparative study of the efficiency of twisted and flat flapping wings during hovering flight. *Bioinspir. Biomim.* **12**, 036009.

Qiu, A., Albert, M., Younes, L. and Miller, M. I. (2009). Time sequence diffeomorphic metric mapping and parallel transport track time-dependent shape changes. *NeuroImage* **45**, S51–S60.

Ravi, S., Crall, J. D., McNeilly, L., Gagliardi, S. F., Biewener, A. A. and Combes, S. A. (2015). Hummingbird flight stability and control in freestream turbulent winds. *Journal of Experimental Biology* **218**, 1444–1452.

Ravi, S., Noda, R., Gagliardi, S., Kolomenskiy, D., Combes, S., Liu, H., Biewener, A. A. and Konow, N. (2020). Modulation of Flight Muscle Recruitment and Wing Rotation Enables Hummingbirds to Mitigate Aerial Roll Perturbations. *Current Biology* **30**, 187-195.e4.

Rayner, J. M. V. (1988). Form and Function in Avian Flight. In *Current Ornithology* (ed. Johnston, R. F.), pp. 1–66. Springer US.

Read, T. J. G., Segre, P. S., Middleton, K. M. and Altshuler, D. L. (2016). Hummingbirds control turning velocity using body orientation and turning radius using asymmetrical wingbeat kinematics. *J R Soc Interface* **13**,.

Reynolds, K. V., Thomas, A. L. R. and Taylor, G. K. (2014). Wing tucks are a response to atmospheric turbulence in the soaring flight of the steppe eagle Aquila nipalensis. *Journal of The Royal Society Interface* **11**, 20140645.

Riskin, D. K., Willis, D. J., Iriarte-Díaz, J., Hedrick, T. L., Kostandov, M., Chen, J., Laidlaw, D. H., Breuer, K. S. and Swartz, S. M. (2008). Quantifying the complexity of bat wing kinematics. *Journal of Theoretical Biology* **254**, 604–615.

Riskin, D. K., Iriarte-Díaz, J., Middleton, K. M., Breuer, K. S. and Swartz, S. M. (2010). The effect of body size on the wing movements of pteropodid bats, with insights into thrust and lift production. *J Exp Biol* **213**, 4110–4122.

Riskin, D. K., Bergou, A., Breuer, K. S. and Swartz, S. M. (2012). Upstroke wing flexion and the inertial cost of bat flight. *Proc. R. Soc. B* rspb20120346.

Schlager, S. (2017). Morpho and Rvcg – Shape Analysis in R: R-Packages for Geometric Morphometrics, Shape Analysis and Surface Manipulations. In *Statistical Shape and Deformation Analysis*, pp. 217–256. Academic Press.

Segre, P. S., Dakin, R., Zordan, V. B., Dickinson, M. H., Straw, A. D. and Altshuler, D. L. (2015). Burst muscle performance predicts the speed, acceleration, and turning performance of Anna's hummingbirds. *eLife Sciences* **4**, e11159.

Sholtis, K. M., Shelton, R. M. and Hedrick, T. L. (2015). Field flight dynamics of hummingbirds during territory encroachment and defense. *PLoS ONE* **10**, e0125659.

Simpson, G. L. (2023). gratia: Graceful ggplot-Based Graphics and Other Functions for GAMs Fitted using mgcv.

Skandalis, D. A., Segre, P. S., Bahlman, J. W., Groom, D. J. E., Jr, K. C. W., Witt, C. C., McGuire, J. A., Dudley, R., Lentink, D. and Altshuler, D. L. (2017). The biomechanical origin of extreme wing allometry in hummingbirds. *Nature Communications* **8**, 1047.

Slice, D. E. (2001). Landmark Coordinates Aligned by Procrustes Analysis Do Not Lie in Kendall's Shape Space. *Systematic Biology* **50**, 141–149.

Song, J., Luo, H. and Hedrick, T. L. (2014). Three-dimensional flow and lift characteristics of a hovering ruby-throated hummingbird. *J. R. Soc. Interface* **11**, 20140541.

Song, J., Luo, H. and Hedrick, T. L. (2015). Performance of a quasi-steady model for hovering hummingbirds. *Theoretical and Applied Mechanics Letters* **5**, 50–53.

Standen, E. M. and Lauder, G. V. (2005). Dorsal and anal fin function in bluegill sunfish Lepomis macrochirus: three-dimensional kinematics during propulsion and maneuvering. *Journal of Experimental Biology* **208**, 2753–2763.

Stowers, A. K., Matloff, L. Y. and Lentink, D. (2017). How pigeons couple three-dimensional elbow and wrist motion to morph their wings. *Journal of The Royal Society Interface* **14**, 20170224.

Swartz, S. M., Bishop, K. and Ismael Aguirre, M.-F. (2006). Dynamic Complexity of Wing Form in Bats: Implications for Flight Performance. In *Functional and Evolutionary Ecology of Bats* (ed. Zubaid, A.), McCracken, G. F.), and Kunz, Thomas H.), pp. 110–130. Oxford, UK: Oxford University Press.

Theriault, D. H., Fuller, N. W., Jackson, B. E., Bluhm, E., Evangelista, D., Wu, Z., Betke, M. and Hedrick, T. L. (2014). A protocol and calibration method for accurate multi-camera field videography. *J Exp Biol* **217**, 1843–1848.

Thomas, A. L. R. (1996). The Flight of Birds that have Wings and a Tail: Variable Geometry Expands the Envelope of Flight Performance. *Journal of Theoretical Biology* **183**, 237–245.

Tobalske, B. W., Warrick, D. R., Clark, C. J., Powers, D. R., Hedrick, T. L., Hyder, G. A. and Biewener, A. A. (2007). Three-dimensional kinematics of hummingbird flight. *Journal of Experimental Biology* **210**, 2368–2382.

Tran, A. P., Yan, S. and Fang, Q. (2020). Improving model-based functional near-infrared spectroscopy analysis using mesh-based anatomical and light-transport models. *NPh* **7**, 015008.

Tytell, E. D., Leftwich, M. C., Hsu, C.-Y., Griffith, B. E., Cohen, A. H., Smits, A. J., Hamlet, C. and Fauci, L. J. (2016). Role of body stiffness in undulatory swimming: Insights from robotic and computational models. *Phys. Rev. Fluids* **1**, 073202.

Walker, S. M., Thomas, A. L. R. and Taylor, G. K. (2009). Photogrammetric reconstruction of high-resolution surface topographies and deformable wing kinematics of tethered locusts and free-flying hoverflies. *J. R. Soc. Interface* **6**, 351–366.

Warrick, D. R., Tobalske, B. W. and Powers, D. R. (2005). Aerodynamics of the hovering hummingbird. *Nature* **435**, 1094–1097.

Watanabe, A. (2018). How many landmarks are enough to characterize shape and size variation? *PLOS ONE* **13**, e0198341.

Wells, D. J. (1993). Ecological correlates of hovering flight of hummingbirds. *Journal of Experimental Biology* **178**, 59–70.

Windes, P., Fan, X., Bender, M., Tafti, D. K. and Müller, R. (2018). A computational investigation of lift generation and power expenditure of Pratt's roundleaf bat (Hipposideros pratti) in forward flight. *PLOS ONE* **13**, e0207613.

Wood, S. N. (2017). *Generalized Additive Models: An Introduction with R, Second Edition*. 2nd ed. Boca Raton, FL: CRC Press.

Young, J., Walker, S. M., Bomphrey, R. J., Taylor, G. K. and Thomas, A. L. R. (2009). Details of Insect Wing Design and Deformation Enhance Aerodynamic Function and Flight Efficiency. *Science* **325**, 1549–1552.

Zheng, L., Hedrick, T. L. and Mittal, R. (2013). Time-Varying Wing-Twist Improves Aerodynamic Efficiency of Forward Flight in Butterflies. *PLOS ONE* **8**, e53060.